small structures
www.small-structures.com

Green Hydrogen Production via Water Splitting Using $SrFe_{0.9}Mo_{0.1}O_{3-\delta}$ Perovskite as a Catalyst

Gloria Anemone, María T. Azcondo, Alvaro Muñóz-Noval, Amjad Al Taleb, Juan Rubio-Zuazo, Daniel Farías, and Ulises Amador**

Evidence of hydrogen production from water splitting using a nonstoichiometric cubic perovskite, $SrFe_{0.9}Mo_{0.1}O_{3-\delta}$ (SFMO), as a catalyst under moderate operating condition is presented. It is demonstrated that the SFMO oxide, when reduced at 800 °C in air, can dissociate water to produce hydrogen and oxygen at the same temperature. The direct test of water dissociation with consequent hydrogen production is carried out using quadrupole mass spectrometry (QMS) under ultrahigh vacuum conditions, where the production of hydrogen by the material is unambiguously determined using heavy water. In addition, in operando synchrotron X-ray diffraction and X-ray absorption spectroscopy are employed to track structural and electronic changes during the reaction, revealing a reversible unit cell expansion without oxygen incorporation and indicating a nonredox mechanism distinct from that of conventional perovskites. This combined characterization approach enables correlation between gas-phase evolution and the structural and electronic response of the catalyst. The reaction cycle could be repeated several times without any decomposition, segregation, or irreversible structural changes, demonstrating the high stability of SFMO. These findings highlight SFMO as a robust and stable catalyst for sustainable hydrogen generation, with strong potential for integration into solar-driven water splitting technologies.

1. Introduction

Hydrogen is emerging as a key element in the transition to a clean energy economy. One of its main advantages is its versatility: it can be used both as an energy carrier, that is, as a renewable energy storage medium, and as a clean fuel, with applications in strategic sectors such as industry, transport, and power generation.[1,2] However, despite its potential, producing green hydrogen through sustainable, emission-free methods is currently more expensive than conventional, fossil fuel-based processes. In fact, green hydrogen currently accounts for less than 1% of the total hydrogen produced worldwide. Of the various possible methods of producing green hydrogen on a large scale, water splitting is the cleanest option as it can be integrated with renewable energy sources, such as solar power, thereby eliminating dependence on nonrenewable resources and minimizing environmental impact.[3,4] Among water splitting strategies, electrolysis is the most established

G. Anemone
Department of Mathematics
CUNEF Universidad
28040 Madrid, Spain

M. T. Azcondo, U. Amador
Facultad de Farmacia
Departamento de Química y Bioquímica
Universidad San Pablo-CEU, CEU Universities
Urbanización Montepríncipe, Boadilla del Monte, E-28668 Madrid, Spain
E-mail: uamador@ceu.es

A. Muñóz-Noval
Departamento de Física de Materiales
Facultad de Física
Universidad Complutense
E-28040 Madrid, Spain

The ORCID identification number(s) for the author(s) of this article can be found under https://doi.org/10.1002/sstr.202500544.

DOI: 10.1002/sstr.202500544

A. Muñóz-Noval
IMDEA Nanociencia
Faraday 9, Cantoblanco, 28049 Madrid, Spain

A. Al Taleb, D. Farías
Departamento de Física de la Materia Condensada
Universidad Autónoma de Madrid
28049 Madrid, Spain
E-mail: daniel.farias@uam.es

J. Rubio-Zuazo
SpLine Spanish CRG Beamline
ESRF, Rue J. Horowitz, Grenoble 38042, Isere/Rhone-Alpes, France

J. Rubio-Zuazo
Instituto de Ciencia de Materiales de Madrid-ICMM/CSIC
Sor Juana Inés de la Cruz, 3, 28049 Madrid, Spain

D. Farías
Instituto Nicolás Cabrera and Condensed Matter Physics Center (IFIMAC)
Universidad Autónoma de Madrid
28049 Madrid, Spain

approach, and recent advances in nanoparticle decorated materials and bifunctional non-noble metal electrocatalysts have shown remarkable potential to improve efficiency and reduce costs.[5,6] Thermolysis is another direct and clean method that uses only heat to split water, but it requires extremely high temperatures (>3000 K), which poses major technical challenges.[7] To overcome these limitations, alternative strategies have been developed to split water at lower temperatures, often with the help of catalytic materials that facilitate the reaction through different mechanisms. Among them, solar thermochemical cycles using metal oxides represent a promising approach, as they utilize concentrated solar heat to split water into hydrogen and oxygen. Moreover, these cycles can be adapted to various redox reactions, including CO_2 splitting,[8] demonstrating the versatility of perovskite-based materials in solar-powered fuel production.[9,10]

In this context, nonstoichiometric metal oxides, in particular certain perovskites, have become particularly attractive candidates due to their tunable redox properties, structural stability, and ability to reversibly exchange oxygen under operating conditions. In classical perovskites, with general ABO_3 stoichiometry, water splitting is commonly described by an oxidation–reduction mechanism: the material is first reduced at elevated temperatures, forming oxygen vacancies. Upon exposure to water, these vacancies are filled by oxygen atoms from water molecules, reoxidizing the material and producing hydrogen. A substantial body of literature has reported on the design and optimization of perovskites for such two-step redox cycles, in which redox processes govern catalytic activity.[11–14] Recently, isothermal thermochemical cycles operating at moderate temperatures (≈800 °C) have been proposed as a way to simplify reactor design and improve overall process efficiency by eliminating the need for repeated thermal swings.[15]

The evolution of gases such as H_2 and O_2 in metal oxides has traditionally been attributed to redox mechanisms centered on transition metal cations, such as Fe^{4+}/Fe^{3+}. However, recent studies have revealed alternative mechanisms. For example, Grimaud et al.[16] demonstrated that in highly covalent perovskites, lattice oxygen can actively participate in the oxygen evolution reaction through pathways involving its direct oxidation and decoupled proton and electron transfers, challenging the exclusive role of the metal cation as a redox center. Along the same lines, a recent theoretical study evaluated different reaction pathways for water dissociation in $SrFeO_{3-\delta}$-type perovskites doped with metals at the B site, where it was observed that H_2 evolution can be favored by the presence of surface oxygen vacancies and depends significantly on the type of dopant.[17] These results highlight the possible contribution of surface oxygen vacancies and the local reorganization of metal–oxygen bonds as unconventional reaction pathways in perovskites, including routes in which the oxygen generated is not reincorporated into the crystal lattice, in clear contrast to the typical behavior of a regenerative redox cycle.

In this work, we have directly monitored hydrogen production using in situ quadrupole mass spectrometry (QMS), providing unambiguous evidence of water dissociation on $SrFe_{0.9}Mo_{0.1}O_{3-\delta}$ (SFMO) at high temperature. In parallel, we have used in-operando synchrotron X-ray diffraction (SXRD) and synchrotron X-ray absorption spectroscopy (XAS) to track structural and electronic changes during the process. This dual approach enables us to correlate the evolution of gas-phase species with the material's structural response in real time.

All experiments have been conducted isothermally at moderate temperature (800 °C), without applying thermal ramps or cycling throughout the process. Our findings show that SFMO promotes water dissociation and hydrogen formation without undergoing reoxidation, as indicated by both the absence of oxygen incorporation and the reversible expansion of the unit cell. These results support a nonredox mechanism and highlight SFMO's potential for stable and efficient hydrogen generation under moderate operating conditions.

2. Results and Discussion

2.1. Material Characterization

2.1.1. XRD and SEM at RT

The as-prepared sample is single-phase, as shown in Figure S1, Supporting Information, with the nominal composition (Table S1, Supporting Information) and homogeneous distribution of the constituent elements (Figure S2, Supporting Information). The crystallite size of the pristine sample, determined by Rietveld analysis of the SXRD (Table S2 and Figure S3, Supporting Information), is estimated to be around 914.7(4) Å; although postcombustion annealing induces particle growing, the crystallite size remains in the nanometer range, as is usually achieved by this procedure. SXRD data recorded for this sample under different conditions confirm its purity and the cubic perovskite-like structure and allow complete structural refinement. Figure S3 to S5, Supporting Information, present the graphic results of the data fitting in different conditions (exposure at different atmospheres and temperatures), whereas the corresponding structural parameters are given in Table S1, Supporting Information. Although X-ray diffraction (XRD) is generally less sensitive to light atoms such as oxygen, the high symmetry of the present structure, combined with the fact that only the oxygen occupancy and thermal factors need to be refined, allows good quality SXRD data to fully characterize the material. Therefore, the structural parameters provided in Table S2, Supporting Information, can be considered reliable (see below for a comparison of the information obtained for the same sample at 800 °C in air using SXRD and neutron powder diffraction (NPD)). The as-obtained oxide is cubic, with no order of Fe and Mo in the perovskite B-sites, and with a significant concentration of oxygen vacancies, around 0.11 per formula unit (p.f.u.), in agreement with the composition determined by titration ($SrFe^{3+}_{0.44(1)}Fe^{4+}_{0.46(1)}Mo_{0.10}O_{2.87(2)}$) and with previous results obtained by NPD, where Mo was also reported to chemically and structurally stabilize a high-symmetry perovskite-like derivative of $SrFeO_3$,[18] which shows outstanding electrochemical performances. These properties, due to Mo, were key motivations for selecting this composition in the present work.

2.1.2. Thermal Reduction Study

The thermal reduction of SFMO has been studied using four techniques: thermogravimetry, SXRD, XAS at ambient pressure, and QMS under ultra-high vacuum (UHV) conditions. Heating SFMO in air induces weight loss, beginning around 400 °C and continuing up to at least 1000 °C (see Figure S6, Supporting Information). Fitting the SXRD pattern (Figure S4, Supporting Information), which was collected on a sample heated in air at 800 °C for 1 h, revealed noticeable oxygen loss. The oxygen content was found to be 2.76(2) p.f.u, meaning that the oxide vacancy concentration was 0.24 p.f.u. (Table S2, Supporting Information).

The X-ray absorption near-edge structure (XANES) spectra of the Fe K-edge of SFMO at room temperature (RT) (blue spectrum) and at 800 °C (red spectrum), shown in Figure 4a, present a similar shape and common characteristics. Both spectra show a prepeak in the same position, while the main edge resonances are shifted slightly relative to each other. The main edge resonance of the SFMO compound at 800 °C is shifted to lower energies compared to that at room temperature (see inset in Figure 4a). This suggests that the oxidation state of Fe at 800 °C is slightly lower than at room temperature. These observations are further supported by the first derivative spectra in Figure 4b. The maximum of the derivative curve corresponds to the inflection point of the absorption edge, which is a sensitive indicator of edge energy. This maximum appears at a slightly lower energy in the 800 °C spectrum. This confirms the downshift of the edge seen in Figure 4a, reinforcing the conclusion that Fe is partially reduced upon heating. It should also be noted that the higher intensity of the main peak at the edge of the room temperature spectrum may be due to the Fe cations having a more symmetrical local order in the structure than at 800 °C.[19] Another contributing factor is the thermal expansion of the material, which can also explain the decrease in white line intensity observed at 800 °C compared to that recorded at room temperature. As the crystal lattice expands with temperature, the Fe—O bonds lengthen, reducing the effective interaction between iron and its chemical environment. This weakening of the coordination environment causes a lower localization of the electron in the final absorption state, which manifests itself as a reduction in the intensity of the white lines in the XANES spectrum.[20,21]

It is known that oxides with metals with variable oxidation states can lose oxygen when heated (even in air), so the molar volume may increase by two mechanisms: through thermal expansion, or due to cation reduction associated with oxygen release. To study the behavior of SFMO, SXRD patterns have been taken in air as a function of temperature in the range between 25 and 800 °C. As shown in **Figure 1**, the lattice constant increases with increasing temperature, but not uniformly, showing a change of trend at 300 °C. This change could be due to a phase transition (e.g., from cubic to tetragonal). However, no evidence of such a transition is detected in either SXRD or XAS measurements. Instead, at this temperature, the perovskite begins to lose oxygen, leading to noticeable expansion of the crystal lattice. Consequently, in addition to thermal expansion, the contribution of chemical expansion must also be considered. This type of expansion, known as stoichiometric expansion,

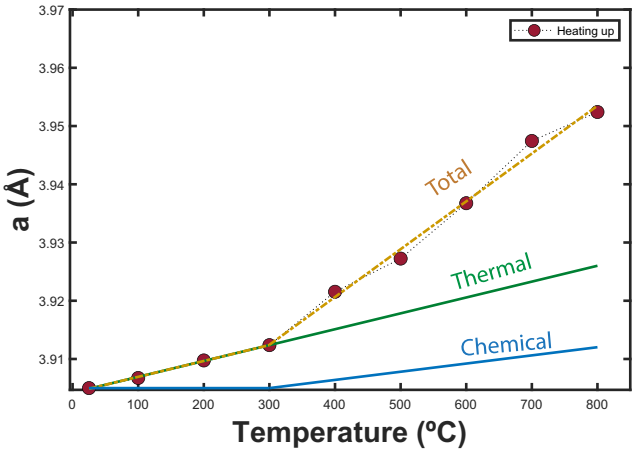

Figure 1. Lattice parameter expansion of SFMO in air during heating at various temperatures (red circles), as measured by SXRD. The graph also includes the calculated contributions of thermal and chemical expansion to the total expansion (see text for details).

refers to chemical expansion in nonstoichiometric oxides, where lattice expansion is driven by a reduction in oxygen content.[22,23] Reduction of cations from a higher to a lower valence state (e.g., Fe^{4+} to Fe^{3+}) can further contribute to expansion due to an increase in ionic radius.[24]

To quantify the two contributions, two linear fits were performed: one for the temperature range of 25–300 °C and another for 300–800 °C. The linear thermal expansion coefficient (TEC) can be directly determined from the slope of the line that best fits the data in the 25–300 °C range (green line in Figure 1).

The linear TEC is defined as follows: $\alpha_T = \frac{1}{a_0}\frac{\partial a}{\partial T}$, where a_0 is the initial lattice constant, taken as the reference value. Taking a_0 as the value at 25 °C ($a_0 = 3.905$Å) yields a value for α_T of $6.977 \cdot 10^{-6}$ °C^{-1}. By fitting the second temperature range, we can determine the total expansion coefficient, which takes into account both thermal and chemical expansion contributions. The total coefficient in this case is $2.1025 \cdot 10^{-5}$ °C^{-1}. The thermal expansion at high temperatures follows the same trend as in the lower temperature range. This is because, when the temperature is significantly higher than the Debye temperature, the thermal expansion coefficient is considered to be constant.[25] In similar materials, such as $SrFeO_3$, the Debye temperature has been estimated to be below 380 K.[26,27] Therefore, in the high-temperature range, we can assume the same expansion coefficient as in the lower-temperature range. By subtracting the previously determined TEC from the total expansion, we obtain the chemical expansion coefficient, calculated as $1.405 \cdot 10^{-6}$ °C^{-1}. On cooling, the material contracts following the same trend observed on heating (Figure S7, Supporting Information). However, within the temperature range of 25–400 °C, the contraction is more pronounced than the expansion. This may be due to increased structural order within the perovskite framework and vacancy rearrangement during oxygen uptake, which fills the vacancies generated at high temperature. In addition, the smaller unit cell reached at RT upon cooling suggests that some vacancies present in the as-prepared material

are filled during the slow cooling process employed in the thermo-diffraction experiment.

2.2. Water-Splitting

2.2.1. Hydrogen Detection

To directly monitor the hydrogen production and the evolution of other products from the water dissociation reaction, in situ QMS was employed under UHV conditions during the annealing process of SFMO, as well as during water exposure. Initially, the sample was heated to 800 °C to induce the reduction of the material, leading to oxygen loss and, consequently, the vacancy formation. At the same temperature, heavy water (D_2O) was introduced into the chamber at a partial pressure of 2×10^{-7} mbar for 5 min. **Figure 2** shows the mass spectra obtained under UHV conditions before (red spectrum) and after (blue spectrum) exposure of the SFMO sample to heavy water. After water introduction, a clear peak is detected at mass 4 (m/e = 4), corresponding to D_2 molecules. This is most clearly seen in the inset of Figure 2, where a weaker peak can also be observed at mass 3 (m/e = 3), corresponding to HD molecules formed due to residual H_2 in the chamber, albeit at very low levels. Evidence of an increase in the oxygen peaks, both atomic (m/e = 16) and molecular (m/e = 32), is also observed. Following water exposure, peaks at masses 20 (m/e = 20) and 18 (m/e = 18), indicative of D_2O in the chamber, remain detectable in the spectrum. This detection persists due to the time required for the pumps to fully evacuate the chamber of water. To exclude the possibility that water dissociation originated from sample holder, the experiment was repeated without the SFMO sample. As can be seen from the spectra in Figure S8, Supporting Information, the contribution of the sample holder is negligible. Therefore, our data suggest that the water molecule is undergoing dissociation, resulting in the production of hydrogen and oxygen, with the SFMO acting as a catalyst.

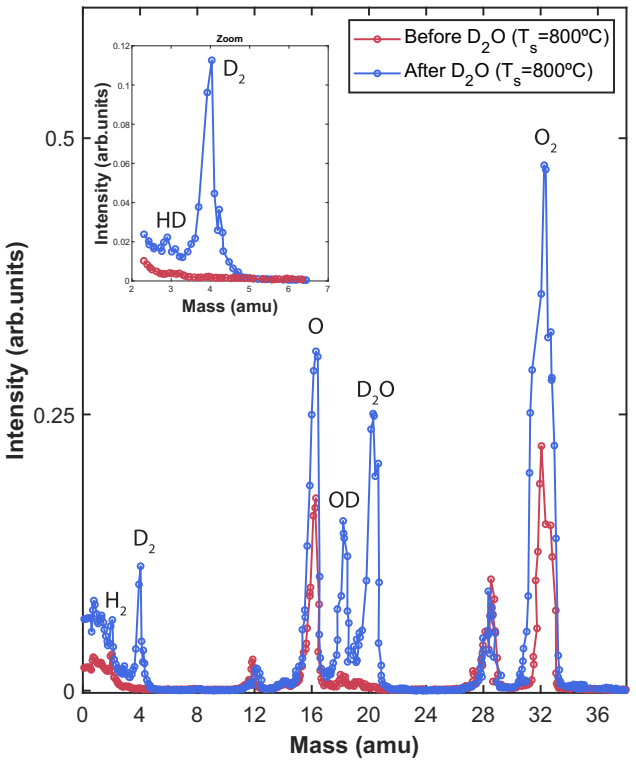

Figure 2. A comparison of the mass spectra of the residual gases in the chamber before (red spectrum) and after (blue spectrum) the exposure of SFMO to D_2O.

2.2.2. Insight into the Water-Splitting Mechanism

In similar perovskites of general ABO_3 stoichiometry, it has often been assumed that the dissociation of water occurs through an oxidation–reduction mechanism of the material.[13,28,29] In the first stage of the process, the material is reduced, resulting in the formation of oxygen vacancies. When water is then introduced, the oxygen atoms in the water molecule occupy these vacancies, which allows the material to be reoxidized and molecular hydrogen (H_2) to be produced. However, according to our experimental evidence, this is not the mechanism responsible for water dissociation on SFMO under the aforementioned experimental conditions. In fact, we observe that the material loses oxygen when heated to 800 °C under UHV conditions, as shown in **Figure 3**a, but the initial oxygen intensity is never recovered during water exposure, indicating that the material is not reoxidized.

To further test this hypothesis, a follow-up experiment was conducted in which the reduced sample was exposed to molecular oxygen instead of water, under the same temperature and pressure conditions. If the oxygen vacancies were active and available for reoxidation, a noticeable change in the oxygen-related peaks would be expected. Oxygen was introduced at a partial pressure of 2×10^{-7} mbar for 5 min, while maintaining the sample at 800 °C. Figure 3b illustrates the spectra before (red spectrum) and after (yellow spectrum) O_2 exposure. Immediately after the O_2 was removed, no change in the intensity of the oxygen peaks (both atomic and molecular) was observed. This suggests that the vacancies have not been filled. Otherwise, the desorption of oxygen and subsequent reduction of the material would have been visible in the spectrum following the O_2 exposure. This confirms that, under the same temperature and pressure conditions used for the water experiments, molecular oxygen, often regarded as a stronger oxidizing agent in many redox processes,[30] does not reoxidize the material.

To complement the QMS results, in operando XANES spectroscopy was employed to investigate the redox behavior and local structural changes of Fe and Mo atoms. The evolution of the Fe K-edge from room temperature to 800 °C in air (blue to red spectra in **Figure 4**a,b) has been previously described in this work, where a slight edge shift to lower energy was associated with a reduction of Fe and a loss of local symmetry upon heating. Here, we focus on the influence of H_2O at high temperature, as seen in the green and yellow spectra of Figure 4a. These spectra exhibit a clear increase in white-line intensity compared to the dry 800 °C sample (red), which approaches the RT one (blue). This suggests a partial restoration of local symmetry or coordination around Fe cations, likely due to structural reordering or oxygen incorporation. However, the first derivative spectra in Figure 4b show that the edge position remains unchanged between the dry and humid 800 °C samples, and does not return

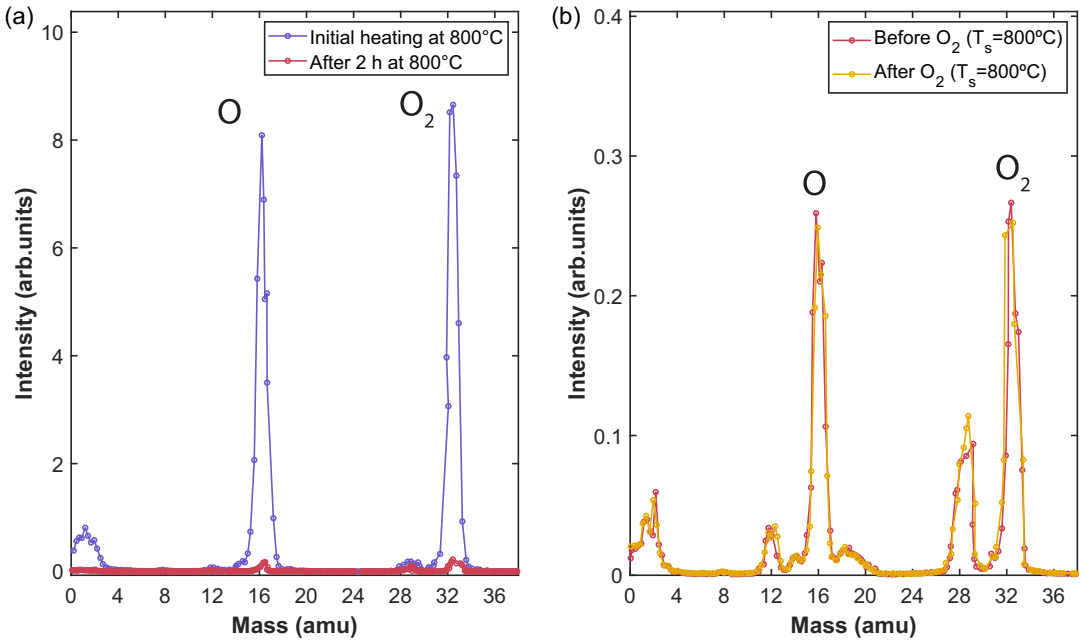

Figure 3. a) Mass spectra recorded during the initial heating at 800 °C (purple curve) and after keeping the sample for 2 h at the same temperature (red curve). A pronounced release of atomic and molecular oxygen is observed in the purple spectrum. b) A comparison of mass spectra recorded before (red curve) and after (yellow curve) O_2 exposure at 800 °C, showing no change in the intensity of the oxygen peaks.

to the higher energy characteristic of the RT condition. We observe a clear increase in the intensity of the Fe K-edge pre-edge feature upon exposure to H_2O at 800 °C (green and yellow spectra in the inset of 4a), while the edge position remains unchanged. This enhancement of the pre-edge is typically associated with a decrease in the local symmetry around the absorbing atom, enabling greater 3d–4p orbital mixing and thus enhancing the dipole-forbidden 1s → 3d transition.[19,31] Since the edge energy remains constant, this change is not linked to a variation in oxidation state, but rather to a modification of the Fe coordination environment. Notably, the pre-edge intensity of the sample treated at 800 °C in dry air (red) is nearly identical to that of the room temperature reference (blue), indicating that thermal treatment alone does not significantly change the coordination environment or generate sufficient oxygen vacancies to affect the pre-edge region. Therefore, the observed pre-edge enhancement under H_2O exposure cannot be attributed to further oxygen loss and the increase in white-line intensity cannot be ascribed to either an actual increase in symmetry or to a reoxidation of the material. A more plausible explanation is that the effect arises from a symmetry-breaking mechanism specifically induced by the presence of H_2O, possibly associated with the formation of surface –OH groups, as reported for hematite under humid conditions,[32,33] which could modify the Fe–ligand environment and contribute to the observed spectral changes.

By contrast, the Mo K-edge spectra (Figure 4c,d) demonstrate remarkable stability across all experimental conditions. Spectra collected at room temperature in air, at 800 °C in air, and at 800 °C in water reveal no significant shift in the absorption edge or white-line intensity. Further confirmation of the absence of any edge shift is provided by the first derivative curves, which indicate that the oxidation state and coordination environment of Mo remain unchanged, even under exposure to water. Mo acts as a redox-inactive element in the oxide, maintaining its high oxidation state (likely Mo^{6+} in octahedral coordination).

In operando SXRD measurements were performed to assess whether any structural changes associated with reoxidation could be detected. Figure S4 and S5, Supporting Information, show SXRD patterns of SFMO perovskite taken at 800 °C reduced in air and during H_2O exposure, respectively. The fitting of these data confirmed that the material retains a cubic perovskite-like structure, with no formation of secondary. To detect possible changes in the unit cell size due to the different treatments, the (321) diffraction peak, one of the most intense at high diffraction angles and highly sensitive to variations in lattice parameters, was monitored, as shown in **Figure 5**a. As can be seen, this peak shifts when the material is exposed to water at 800 °C. Upon introducing water, the peak moves to lower angles, indicating an expansion of the unit cell (Figure 5b). It is generally accepted that, when a material undergoes reoxidation during exposure to water, the unit cell is expected to contract, resulting in a shift of the peak to higher diffraction angles. However, the experimental results summarized in Figure 5a suggest a different mechanism at play. From the spacing of the (321) peak, it is possible to determine the unit cell parameter and its evolution throughout the experiment. Figure 5b illustrates how the peak moves during the two-stage process during one cycle (the first one is used as an example). Figure 5c shows the evolution of the lattice constant parameter as a function of time along the experiment. Once the water flow has been cut off and a dry air stream is applied, the peak returns to its initial position, that is, the lattice constant decreases back to the value it had before the water was introduced. This confirms that the structural change is fully reversible.

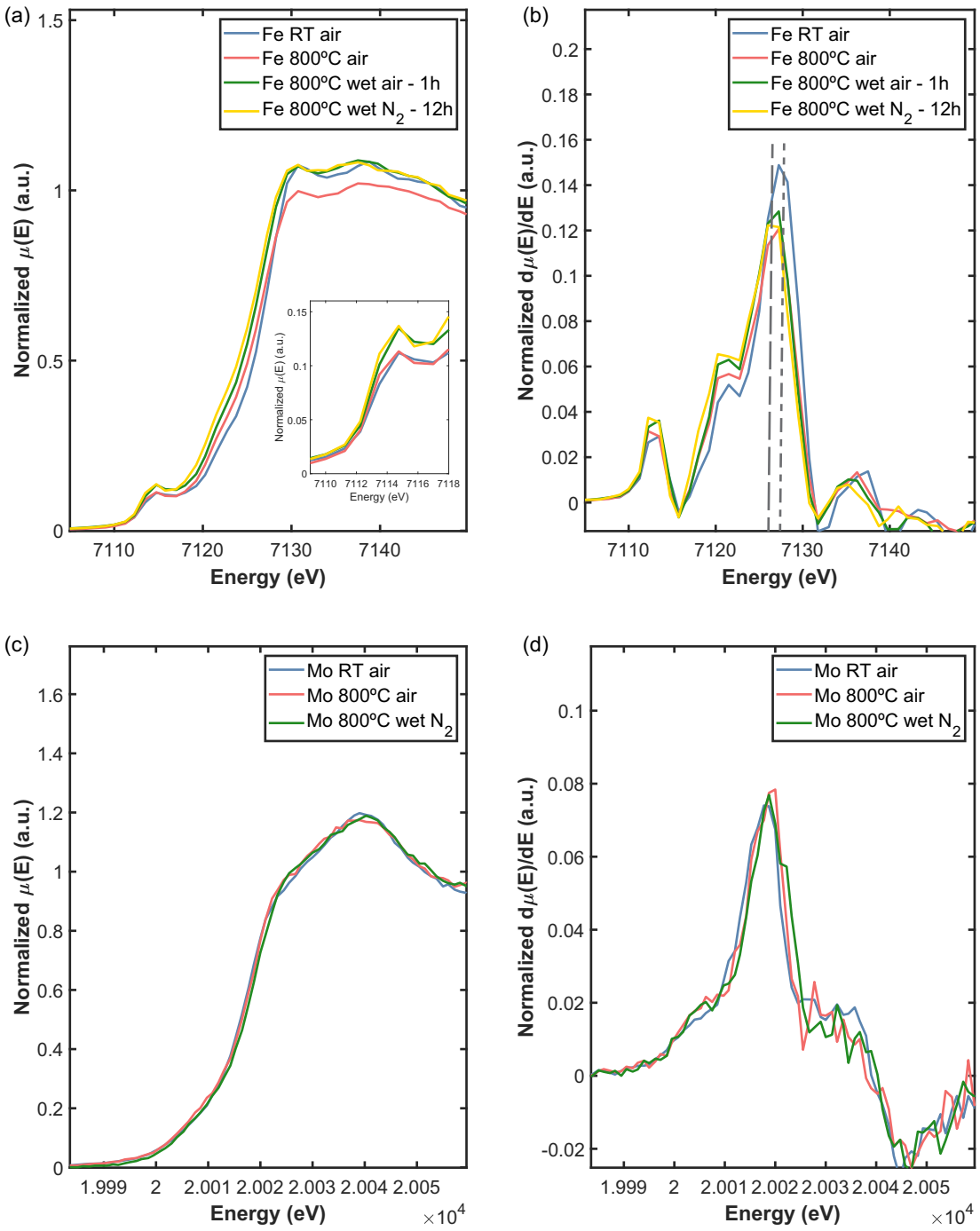

Figure 4. XANES spectra and their first derivatives for Fe and Mo under different conditions. a) Normalized Fe K-edge absorption spectra and b) their first derivative for samples at RT and after heating at 800 °C in air, with and without H_2O exposure. The inset shows a magnified view of the pre-edge region. c) Normalized Mo K-edge absorption spectra and d) their first derivative for samples at RT and after heating at 800 °C in air, with and without H_2O exposure.

These results further support the conclusion that water molecules interacting with the perovskite do not reoxidize the material by filling the oxygen vacancies. If reoxidation were occurring, a lattice contraction would be expected, which is inconsistent with the observed expansion. Further experimental and theoretical studies are essential to shed light on the mechanism governing the water splitting reaction in this material.[34–36]

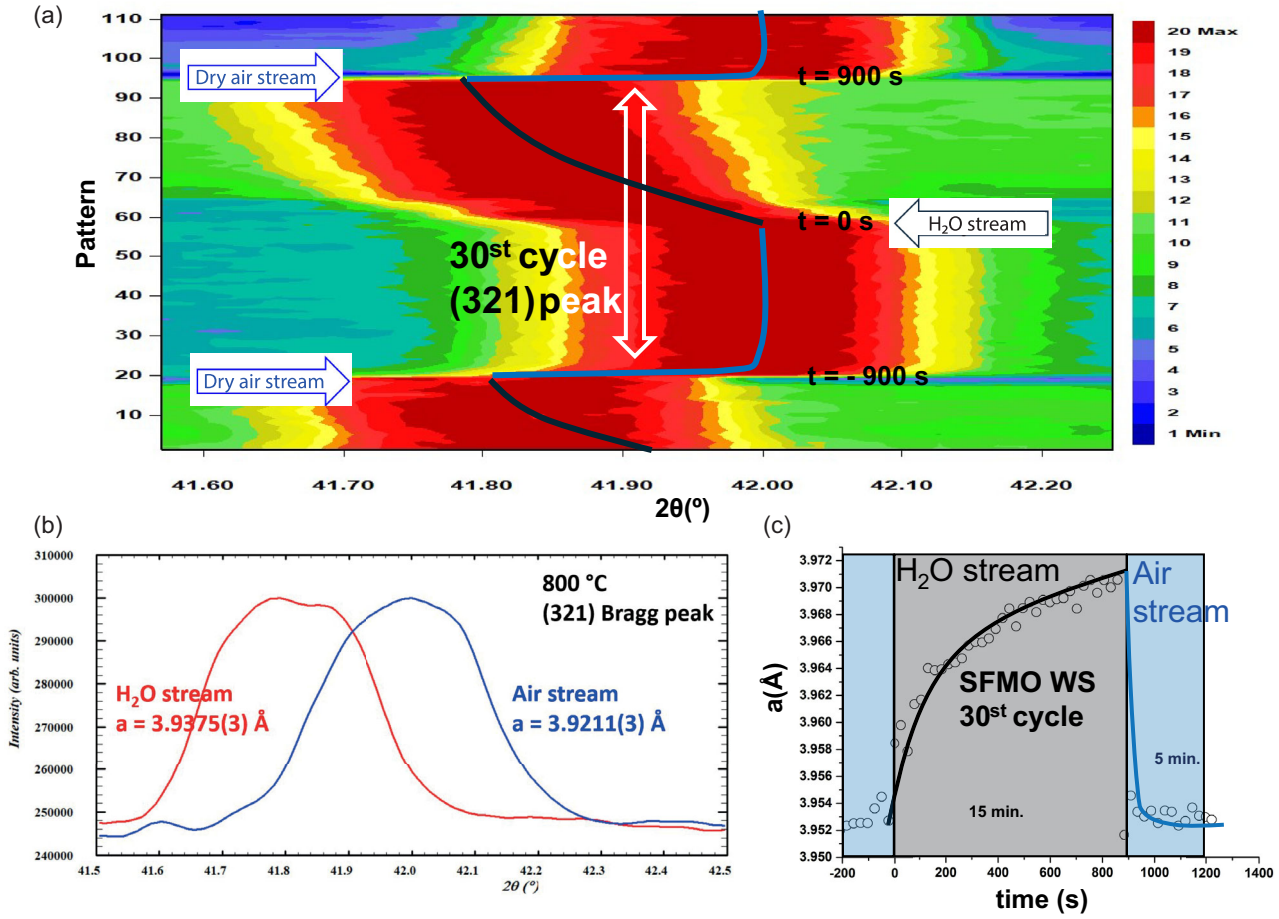

Figure 5. a) Evolution of the (321) peak during the 30th cycle taken at 800 °C. b) (321) peak shift of SXRD pattern of SFMO perovskite taken at 800 °C reduced in air (blue line) and H_2O atmosphere (red line). c) Lattice constant expansion/contraction of SFMO during 2-step cycles.

2.2.3. Structural Stability

To evaluate the structural stability of the material under repeated exposure to water, SXRD measurements were performed in operando over the course of 30 consecutive cycles at ambient pressure. The same procedure was applied in each cycle to ensure consistency. Figure 5a shows the evolution of the unit cell parameter obtained during the 30th cycle. The results indicate that the material maintains its structural integrity throughout the whole cycling process. This reversible multi-cycle behavior is consistent with the stabilizing effect of Mo, as anticipated when selecting this composition. Notably, the (321) reflection consistently shifts to lower angles upon water exposure, confirming the reproducibility of the structural response. Additionally, the data confirm that the expansion of the unit cell upon contact with water is reversible and stable over repeated cycles. It is worth emphasizing that the entire process takes place at a constant and moderate temperature of 800 °C. No additional heating or cooling steps are required to initiate or reverse water dissociation, indicating that the observed structural and chemical changes occur purely as a result of the interaction between water and the material under isothermal conditions. Furthermore, postreaction XRD and SEM characterization carried out after the 30th cycle (see Figure S9 and S10, Supporting Information) confirmed the retention of the cubic perovskite structure and particle morphology, with no signs of degradation, phase segregation, or structural hysteresis, thereby fully supporting the stability claim derived from the in operando SXRD data.

3. Conclusion

In this work, we provide clear evidence that the perovskite $SrFe_{0.9}Mo_{0.1}O_{3-\delta}$ is able to dissociate water, producing molecular hydrogen and oxygen at a relatively low temperature (800 °C). This suggests a promising route to green hydrogen production that could potentially use solar radiation as an energy source. Furthermore, the mechanism appears to differ from the conventional redox process typically associated with this type of perovskite, challenging existing assumptions in the field. Additionally, our results indicate that the material exhibits remarkable structural stability after multiple reaction cycles, maintaining its integrity without undergoing significant decomposition or irreversible structural changes. This makes it a robust candidate for practical and scalable hydrogen production.

4. Experimental Section

Synthesis: The perovskite $SrFe_{0.9}Mo_{0.1}O_{3-\delta}$ was synthesized via the combustion method. Stoichiometric amounts of $Sr(NO_3)_2$ (Sigma–Aldrich, ≤99%), $Fe(NO_3)_3{\cdot}9H_2O$ (Merck, analytical grade), and $(NH_4)_6Mo_7O_24{\cdot}4H_2O$ (Sigma–Aldrich) were mixed, along with glycine as the fuel, to achieve a balanced oxidizer-to-fuel molar ratio based on the nitrate (NO_3^-) content and glycine. The oxidizer-to-fuel equivalence ratio was fixed at 1:1. The concentrated solution of precursors and fuel was placed in a furnace at 500 °C for 30 min to initiate combustion. The resulting combustion ashes were then pressed into pellets and calcined at 1300 °C for 48 h.

Material Characterization: Purity of the pristine samples was determined by XRD on a Bruker D8 high-resolution diffractometer using monochromatic CuKα_1 radiation ($\lambda = 1.5406$ Å) obtained with a germanium monochromator. Rietveld refinements were performed with the Fullprof program[37] on diffraction data collected in the range $20° \leq 2\theta \leq 150°$ ($Q(Å^{-1})$ range 1.41–7.88) with a step-width of 0.015° and a step counting time of 5 s. The instrumental resolution function was determined using a certified standard sample of LaB6 from the USA National Institute of Standards and Technology (NIST).

Chemical composition and elemental maps have been performed using a Prisma-E scanning electron microscope, equipped with electron-dispersive spectroscopy (EDS), employing an UltraDry Premium EDS detector with 129 eV resolution.

The iron oxidation state and oxygen content (assuming charge neutrality) of the pristine sample were determined by titration using potassium dichromate, as described in ref. [38]. Besides, oxygen release as a function of temperature was determined by TGA in air from RT to 1000 °C using a TA Instrument TGA apparatus SDT Q600 at a heating rate of 5 K min^{-1}.

Structural Characterization under Working Conditions: SXRD experiments were performed on the Spline BM25 beamline at the European Synchrotron Radiation Facility (ESRF) using a radiation wavelength of $\lambda = 0.75140$ Å, determined using a certified standard sample of LaB^6 from NIST. The same sample was used to obtain the instrumental resolution function required for microstructural characterization.

Different kinds of experiments were conducted. The SXRD pattern of the pristine material was recorded in the 2θ-range from 10° to 55° ($Q(Å^{-1})$ range 1.46–7.72) to enable structural refinement. Patterns were recorded under the same conditions for the sample at 800 °C in both air and wet nitrogen atmospheres, after stabilization for 1 h. The instrumental resolution function was determined using a certified standard sample of LaB^6 from the USA National Institute of Standards and Technology (NIST).

In-operando SXRD experiments were conducted using a reaction cell Anton Paar DHS 1100. Two-stage WS cycles were performed in isothermal conditions at 800 °C; the duration of the activation/regeneration steps under air and the water splitting stage (under a nitrogen stream saturated with water at 60 °C) were fixed to 15 min (900 s). A gas flux of 100 mL min^{-1} was applied to both stages using the appropriate mass flow controllers. Home-made software was used to control the duration of each stage, the gas flux, and the programmed number of cycles. The (123) peak was continuously monitored (a pattern in the 2θ-range 41.1–42.4° was recorded every 26 s). This peak is sufficiently strong to provide statistically reliable information and appears at a 2θ-angle high enough to allow detecting slight variations of the unit cell along the reaction process.

X-ray absorption near-edge spectroscopy (XANES) measurements were performed on the Spline BM25 beamline at the European Synchrotron Radiation Facility (ESRF). The spectra were recorded in fluorescence yield mode at the Fe K-edge (7112 eV) and Mo K-edge (20 000 eV), averaging a minimum of three spectra adjusting the experimental conditions to achieve a good signal-to-noise ratio. Spectra were collected on the pristine material at RT and at 800 °C under air using the Anton Paar DHS 1100 reaction cell. XANES data were analyzed using the Demeter software package.[39]

Quadrupole Mass Spectrometry: The hydrogen and oxygen production were investigated using a quadrupole mass spectrometer (Mod. Balzers QMG 511) located in a UHV chamber.[40] The synthesized SFMO powder was compressed into a cylindrical pellet with a diameter of 10 mm and a thickness of ≈1 mm using a uniaxial hydraulic press. The pellet was then placed in a molybdenum sample holder and transferred into the QMS chamber. The sample can be cooled down to 90 K using liquid nitrogen and heated by electronic bombardment. A type C thermocouple spot welded to the sample was used to measure the sample temperature. The gases used were D_2O and O_2, which were introduced through leak valves to allow precise dosing of the gases. The dissociation of water molecules in UHV conditions has been performed using D_2O, to ensure that the hydrogen molecules observed in the gas phase come exclusively from the dissociation of water, as there is no background in the UHV chamber for $m/e = 4$, whereas there is for $m/e = 2$.

Supporting Information

Supporting Information is available from the Wiley Online Library or from the author.

Acknowledgements

The authors thank "MCIN/AEI/10.13039/501100011033 and Fondo Europeo de Desarrollo Regional" (FEDER/UE "Una manera de hacer Europa") for funding the project PID2022-139501OB-C21. The authors also thank BM5 Spline line and CSIC for allocating beamtime and facilitating the access to ESRF for XAS and SXRD experiments, through grants A25-2-1017, A25-2-1076, MA-4722, and IH-CH-1546. M.T.A. and U.A. also thank USP-CEU for financial support. This work has been partially supported by the Spanish Ministerio de Ciencia e Innovación under project PID2023-147466OB-C21. The COST Action CA21101 is also acknowledged. D.F. acknowledges financial support from the Spanish Ministry of Economy and Competitiveness, through the "Mara de Maeztu" Programme for Units of Excellence in R&D (CEX2023-001316-M). AMN thanks the project PID2021-126323OA-I00.

Conflict of Interest

The authors declare no conflict of interest.

Author Contributions

Gloria Anemone: investigation (equal); methodology (lead); writing—review and editing (lead). **María T. Azcondo**: conceptualization (equal); funding acquisition (equal); investigation (equal); supervision (equal); writing—original draft (equal). **Alvaro Muñóz-Noval**: data curation (equal); formal analysis (equal); validation (equal). **Amjad Al Taleb**: data curation (equal); methodology (equal); software (lead). **Juan Rubio-Zuazo**: data curation (equal); formal analysis (equal); methodology (equal); resources (equal); validation (equal). **Daniel Farías**: funding acquisition (equal); investigation (equal); resources (equal); writing—original draft (equal). **Ulises Amador**: funding acquisition (equal); investigation (equal); supervision (equal); writing—original draft (equal).

Data Availability Statement

The data that support the findings of this study are available from the corresponding author upon reasonable request.

Keywords

catalysis, green hydrogen, nonstoichiometric perovskites, water-splitting

Received: August 14, 2025
Revised: September 20, 2025
Published online: October 26, 2025

[1] H. Ishaq, I. Dincer, C. Crawford, *Int. J. Hydrogen Energy* **2022**, *47*, 26238.
[2] P. Halder, M. Babaie, F. Salek, N. Haque, R. Savage, S. Stevanovic, T. A. Bodisco, A. Zare, *Int. J. Hydrogen Energy* **2024**, *52*, 973.
[3] S. S. Kumar, H. Lim, *Energy Rep.* **2022**, *8*, 13793.
[4] H. Zhao, L. Jian, M. Gong, M. Jing, H. Li, Q. Mao, T. Lu, Y. Guo, R. Ji, W. Chi, Y. Dong, Y. Zhu, *Small Struct.* **2022**, *3*, 2100229.
[5] T. Wu, M.-Z. Sun, B.-L. Huang, *Rare Metals* **2022**, *41*, 2169.
[6] R. Liu, M. Sun, X. Liu, Z. Lv, X. Yu, J. Wang, Y. Liu, L. Li, X. Feng, W. Yang, B. Huang, B. Wang, *Angew. Chem. Int. Ed.* **2023**, *62*, e202312644.
[7] C. Perkins, A. W. Weimer, *Int. J. Hydrogen Energy* **2004**, *29*, 1587.
[8] L. Wei, Z. Pan, X. Shi, O. C. Esan, G. Li, H. Qi, Q. Wu, L. An, *Iscience* **2023**, *26*, 11.
[9] Y. Bao, F. Zhang, *Small Struct.* **2022**, *3*, 2100226.
[10] M. Li, F. Li, J. Gong, T. Zhang, F. Gao, W.-H. Zhang, M. Liu, *Small Struct.* **2022**, *3*, 2100102.
[11] J. R. Scheffe, A. Steinfeld, *Mater. Today* **2014**, *17*, 341.
[12] A. Demont, S. Abanades, E. Beche, *J. Phys. Chem. C* **2014**, *118*, 12682.
[13] X. Qian, J. He, E. Mastronardo, B. Baldassarri, C. Wolverton, S. M. Haile, *Chem. Mater.* **2020**, *32*, 9335.
[14] J. T. Tran, K. J. Warren, S. A. Wilson, C. L. Muhich, C. B. Musgrave, A. W. Weimer, *Wiley Interdiscip. Rev. Energy Environ.* **2024**, *13*, e528.
[15] M. T. Azcondo, M. Orfila, J. Marugán, R. Sanz, A. Muñoz-Noval, E. Salas-Colera, C. Ritter, F. Garca-Alvarado, U. Amador, *ChemSusChem* **2019**, *12*, 4029.
[16] A. Grimaud, O. Diaz-Morales, B. Han, W. T. Hong, Y.-L. Lee, L. Giordano, K. A. Stoerzinger, M. T. Koper, Y. Shao-Horn, *Nat. Chem.* **2017**, *9*, 457.
[17] S. Chen, H. Cheng, Y. Liu, X. Xiong, Q. Sun, Q. Xu, X. Lu, S. Li, *Phys. Chem. Chem. Phys.* **2022**, *24*, 28975.
[18] V. Zapata-Ramrez, G. C. Mather, M. T. Azcondo, U. Amador, D. Pérez-Coll, *J. Power Sources* **2019**, *437*, 226895.
[19] A. Corrias, G. Ennas, G. Mountjoy, G. Paschina, *Phys. Chem. Chem. Phys.* **2000**, *2*, 1045.
[20] A. Kuzmin, J. Chaboy, *IUCrJ* **2014**, *1*, 571.
[21] G. Bunker, *Introduction to XAFS: A practical guide to X-ray absorption fine structure spectroscopy*, Cambridge University Press **2010**.
[22] S. Bishop, D. Marrocchelli, C. Chatzichristodoulou, N. Perry, M. Mogensen, H. Tuller, E. Wachsman, *Annu. Rev. Mater. Res.* **2014**, *44*, 205.
[23] N. H. Perry, J. J. Kim, S. R. Bishop, H. L. Tuller, *J. Mater. Chem. A* **2015**, *3*, 3602.
[24] D. Marrocchelli, N. H. Perry, S. R. Bishop, *Phys. Chem. Chem. Phys.* **2015**, *17*, 10028.
[25] D. S. Tsvetkov, V. V. Sereda, D. A. Malyshkin, I. L. Ivanov, A. Y. Zuev, *J. Mater. Chem. A* **2022**, *10*, 6351.
[26] H. Rached, D. Rached, M. Rabah, R. Khenata, A. H. Reshak, *Phys. B* **2010**, *405*, 3515.
[27] T. Jia, Z. Zeng, H. Q. Lin, Y. Duan, P. Ohodnicki, *RSC Adv.* **2017**, *7*, 38798.
[28] X. Qian, J. He, E. Mastronardo, B. Baldassarri, W. Yuan, C. Wolverton, S. M. Haile, *Matter* **2021**, *4*, 688.
[29] R. B. Wexler, G. Sai Gautam, R. T. Bell, S. Shulda, N. A. Strange, J. A. Trindell, J. D. Sugar, E. Nygren, S. Sainio, A. H. McDaniel, D. Ginley, E. A. Carter, E. B. Stechel, *Energy Environ. Sci.* **2023**, *16*, 2550.
[30] Z. Chen, Z. Sun, X. Chen, Y. Wu, X. Niu, Y. Song, *Comput. Mater. Sci.* **2021**, *195*, 110475.
[31] T. E. Westre, P. Kennepohl, J. G. DeWitt, B. Hedman, K. O. Hodgson, E. I. Solomon, *J. Am. Chem. Soc.* **1997**, *119*, 6297.
[32] S. Yamamoto, T. Kendelewicz, J. T. Newberg, G. Ketteler, D. E. Starr, E. R. Mysak, K. J. Andersson, H. Ogasawara, H. Bluhm, M. Salmeron, G. E. Brown, Jr., A. Nilsson, *J. Phys. Chem. C* **2010**, *114*, 2256.
[33] E. Voloshina, *Reference Module In Chemistry, Molecular Sciences And Chemical Engineering*, Elsevier **2017**.
[34] M. Riva, M. Kubicek, X. Hao, G. Franceschi, S. Gerhold, M. Schmid, H. Hutter, J. Fleig, C. Franchini, B. Yildiz, U. Diebold, *Nat. Commun.* **2018**, *9*, 3710.
[35] M. P. de Lara-Castells, *Small Struct.* **2024**, *5*, 2400147.
[36] J. Hwang, R. R. Rao, L. Giordano, Y. Katayama, Y. Yu, Y. Shao-Horn, *Science* **2017**, *358*, 751.
[37] J. Rodrguez-Carvajal, *Phys. B* **1993**, *192*, 55.
[38] M. Yuste, J. C. Pérez-Flores, J. R. de Paz, M. T. Azcondo, F. Garca-Alvarado, U. Amador, *Dalton Trans.* **2011**, *40*, 7908.
[39] B. Ravel, M. Newville, *Synchrotron Radiat.* **2005**, *12*, 537.
[40] P. Nieto, D. Barredo, D. Farias, R. Miranda, *J. Phys. Chem. A* **2011**, *115*, 7283.